Micromechanics of sheared granular layers activated by fluid pressurization

Hien Nho Gia NGUYEN[1], Luc Scholtès[2], Yves Guglielmi[3], Frédéric-Victor Donzé[4], Zady Ouraga[5], and Mountaka Souley[5]

[1]Université de Lorraine
[2]Université Clermont-Auvergne
[3]Lawrence Berkeley National Laboratory
[4]Institut des Sciences de la Terre
[5]INERIS

November 26, 2022

Abstract

Fluid pressurization of critically stressed sheared zones can trigger slip mechanisms at work in many geological processes. Using discrete element modeling, we simulate pore-pressure-step creep test experiments on a sheared granular layer under a sub-critical stress state to investigate the micromechanical processes at stake during fluid induced reactivation. The global response is consistent with available experiments and confirms the scale independent nature of fluid induced slip. The progressive increase of pore pressure promotes slow steady creep at sub-critical stress states, and fast accelerated dynamic slip once the critical strength is overcome. Our multi-scale analyses show that these two emergent behaviors correlate to characteristic deformation modes: diffuse deformation during creep, and highly localized deformation during rupture. Creep corresponds to bulk deformation while rupture results from grain rotations initiating from overpressure induced unlocking of contacts located within the shear band which, consequently, acts as a roller bearing for the surrounding bulk.

Micromechanics of sheared granular layers activated by fluid pressurization

Hien Nho Gia Nguyen[1], Luc Scholtès[1,2], Yves Guglielmi[3], Frédéric Victor Donzé[4], Zady Ouraga[5], Mountaka Souley[5]

[1]Université de Lorraine, CNRS, GeoRessources, Nancy, France
[2]Université Clermont Auvergne, CNRS, IRD, OPGC, Laboratoire Magmas et Volcans, Clermont-Ferrand, France
[3]Lawrence Berkeley National Laboratory, Energy Geosciences Division, Berkeley, CA, USA
[4]Université Grenoble-Alpes, CNRS, ISTerre, Grenoble, France
[5]Ineris, Verneuil-en-Halatte, France

Key Points:

- fluid induced reactivation can be either stable or unstable depending on the deformation mode
- slow steady creep is accomodated through distibuted bulk deformation at sub-critical stress states
- accelerated dynamic slip results from intense grain rearrangements localized within the shear band

Corresponding author: Hien Nho Gia Nguyen, nngiahien@gmail.com

Abstract

Fluid pressurization of critically stressed sheared zones can trigger slip mechanisms at work in many geological processes. Using discrete element modeling, we simulate pore-pressure-step creep test experiments on a sheared granular layer under a sub-critical stress state to investigate the micromechanical processes at stake during fluid induced reactivation. The global response is consistent with available experiments and confirms the scale independent nature of fluid induced slip. The progressive increase of pore pressure promotes slow steady creep at sub-critical stress states, and fast accelerated dynamic slip once the critical strength is overcome. Our multi-scale analyses show that these two emergent behaviors correlate to characteristic deformation modes: diffuse deformation during creep, and highly localized deformation during rupture. Creep corresponds to bulk deformation while rupture results from grain rotations initiating from overpressure induced unlocking of contacts located within the shear band which, consequently, acts as a roller bearing for the surrounding bulk.

Plain Language Summary

Fluids can be at the origin of catastrophic disasters, *e.g.*, earthquakes related to deep subsurface fluid injections or lanslides triggered by short-term changes of hydrological conditions. It is now well assumed that these phenomena originate from mechanisms taking place in critically stressed shear zones found along tectonic faults, rock mass fractures or localized deformation bands. The increase of pore pressure promotes slip along these shear zones as confirmed by numerous experimental and numerical studies. In this work, we present computer simulations that reproduce the progressive reactivation of a granular shear zone as a result of fluid pressurization. Our simulations provide grain-scale information that improves understanding of fluid induced slip behaviors and illuminate micromechanical details of phenomenological, macroscale observations.

1 Introduction

Fluid overpressurization is one of the primary mechanisms at the origin of tectonic faults slip (Guglielmi et al., 2015; Cappa et al., 2019), giant landslides evolution (Cappa et al., 2014; Agliardi et al., 2020), or even glaciers deformation (Mathews, 1964; Boulton & Hindmarsh, 1987). In all cases, slip results from mechanisms taking place within localized shear zones where most of the stress is accomodated, and it is now well assumed that these mechanisms are very sensitive to variation of pore pressure due to hydrological forcing, related to either natural or anthropogenic processes. Shear zones in tectonically active faults, at the base of large creeping landslides, or in subglacial beds, are generally sub-critically stressed (i.e., subjected to stress condition slightly lower than their instantaneous strength), and their behavior is directly related to stress related perturbations. Fluid induced reactivation can be interpreted in such a context by considering the effective stress principle combined with Mohr-Coulomb (MC) theory (King Hubbert & Rubey, 1959). Pore fluid pressure variations modify the stress state within the shear zone by reducing the effective normal stress while the shear stress remains constant. Following MC theory and assuming that the strength of the shear zone is known (defined through its cohesion c and friction coefficient μ), the critical stress state τ_c at which failure will occur as a result of fluid pressurization is defined by the following criterion:

$$\tau_c = c + \mu\,(\sigma_N - P) \tag{1}$$

where σ_N is the normal stress acting on the shear zone and P is the pore fluid pressure.

Nonetheless, the MC citerion does not give any information on the mechanisms developing before or after failure. This is rather limiting since shear zones can promote different modes of slip, stable or unstable, sometimes even before the critical sress state is reached (Guglielmi et al., 2015; Scuderi & Collettini, 2016; Scuderi et al., 2017; Cappa

et al., 2019). The rate- and state- friction (RSF) theory offers a sound and well established framework to characterize slip behaviors (Dieterich, 1979; Ruina, 1983; Aharonov & Scholz, 2018). However, even with modifications specifically dedicated to fluid pressure perturbations (Linker & Dieterich, 1992), the RSF theory seems in contradiction with certain behaviors observed in nature (Cappa et al., 2019) or in laboratory (Scuderi et al., 2017). In short, fluid assisted fault reactivation and earthquake triggering cannot be explained in the context of frictional stability analysis for which an increase of fluid pressure should favor stable aseismic slip (Segall & Rice, 1995; Scholz, 1998).

It is now well assumed that shear zones may accumulate displacement in two ways, through either stable creep, or dynamic rupture (Dieterich, 1979; Ruina, 1983). These 2 deformation modes are incidentally related respectively to the aseismic and seismic behaviors used to characterize tectonic faults slip (Reinen, 2000), which have been both observed as a result of fluid pressurization (Cornet et al., 1998). Nonetheless, despite the compelling evidence of slip phenomena caused by pore pressure perturbations, the mechanisms at play remain poorly understood (Scuderi et al., 2017; Scuderi & Collettini, 2018). Indeed, shear zones are more complex than single sliding surface systems. They are generally filled with layers of particulate materials which are commonly termed "gouges" in the tectonic context. The response of such materials to stress perturbations results from frictional sliding, rolling, breaking and rearrangement of grains which are undoubtedly more intricate in the presence of hydromechanical processes.

In this paper, we propose to relate the macroscopic response of a granular shear zone to the micromechanical phenomena at work during fluid induced reactivation. For that matter, we developed a numerical experiment inspired by the experiments performed in (Scuderi et al., 2017) where a sub-critically stressed granular layer is subjected to a progressive pore pressure increase. The numerical experiment is built upon a numerical model based on the discrete element method (DEM) which offers a unique approach to simulate complex emergent behaviors by treating the medium under consideration as an assembly of individual particles interacting one with another according to simplified contact laws (Cundall & Strack, 1979). DEM models have proven effective in producing emergent behaviors representative of fault gouges dynamics for several decades now (Morgan & Boettcher, 1999; Aharonov & Sparks, 2004; Ferdowsi et al., 2013; Ferdowsi & Rubin, 2020). Recent efforts have actually illustrated their capability to investigate friction related fluid coupled processes (Dorostkar et al., 2017; Yang & Juanes, 2018). In this study, we use a hydromechanically coupled DEM model to simulate fluid induced reactivation of a sub-critically stressed shear zone, so as to highlight the micromechanical processes at the origin of the different macroscopic slip behaviors observed.

2 Method

To investigate fluid induced reactivation of sheared granular layers, we utilized a discrete element model coupled with a pore-scale finite volume (PFV) scheme implemented in the YADE DEM software (Šmilauer et al., 2010). The numerical medium consists of a 3D polydisperse assembly of 12,000 spherical particles with a uniform size distribution such that their diameters vary between 0.066mm and 0.133mm. The assembly is enclosed in between two rigid walls in the y direction, and periodic boundaries are defined in both the x and z directions such that particles exit from one side and reappear on the other (Figure 1(a)). This configuration enables to simulate an infinite and homogeneous horizontal layer with a limited computational cost without sacrificing potentially important out of plane particle reorganizations which can be of significance in terms of emerging behaviors (Hazzard & Mair, 2003). Particles interact one with another through elastic-frictional interactions. Each particle is identified by its own mass, radius and moment of inertia. An explicit solution scheme is used to integrate Newton's second law so as to update the particles' positions according to the forces they are subjected to. Compressible fluid flow is modeled within the pore space which is discretized based on a regular

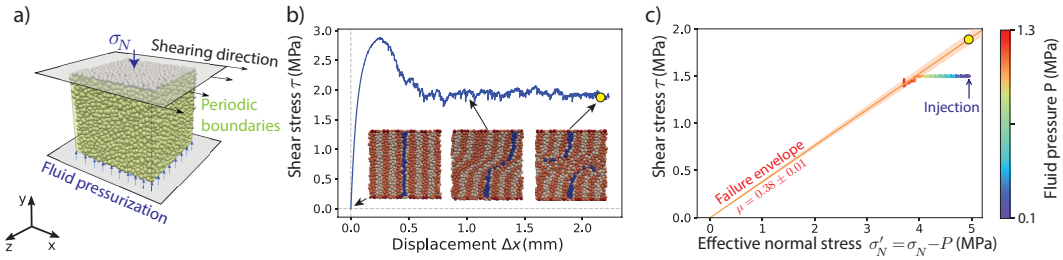

Figure 1. Numerical experiment. (a) DEM model set-up: geometry and boundary conditions defining the granular shear zone. (b) Preconditioning stage: direct shear test to localize shear within the layer. Once the steady-state strength is reached, the shear stress is reduced to 80% of its value prior to fluid injection. (c) Pore-pressure-step creep test: pore fluid pressure is progressively increased under constant shear stress so that the normal effective stress decreases up to failure. The Mohr-Coulomb criterion is plotted for reference.

Delaunay triangulation of the particles' centers (see (Chareyre et al., 2012; Catalano et al., 2014; Scholtès et al., 2015) for details of the implementation). The method is hydro-mechanically coupled in the sense that deformation of the pore space caused by particles' movements induces pore pressure variations and associated interporal flow, while pore pressure changes induce hydraulic forces on the solid particles and associated stress variations. For this study, we considered fluid properties representative of water, with a bulk modulus of 2.2 GPa and a viscosity of 1 mPa.s. The model's parameters and the emergent properties of the simulated shear zone are provided in the supplementary file (Table 1).

The numerical sample is prepared by first hydrostatically compacting a cloud of randomly positioned particles up to 1 MPa (we don't consider gravitational forces in our simulation). The sample is then subjected to a normal stress σ_N of 5 MPa in the y direction through the displacement of the top and bottom walls (the walls are frictionless during this stage). Once equilibrium is reached, the particles in contact with the walls are glued to them in order to produce a certain degree of roughness at the interfaces. The top wall is then translated at a constant displacement rate of $2 \times 10^{-5}\,\mathrm{m\,s^{-1}}$ while the bottom wall is fixed to reach a steady-state strength (Figure 1(b)). This preconditioning stage ensures shear to localize within the simulated medium in the form of a shear band with a thickness of approximately 10 particles, as commonly observed in granular materials (Rattez et al., 2020). Once steady state strength and shear localization are ensured, the top wall is stopped and the control mode changes from displacement-controlled to stress-controlled. Similarly to the creep experiments performed by Scuderi et al. (Scuderi et al., 2017), the shear stress τ is reduced to 80% of the steady state strength τ_{ss} and then kept constant at this sub-critical level while the pore fluid pressure P is increased stepwise to simulate a progressive reduction of the effective normal stress $\sigma'_N = \sigma_N - P$ (Figure 1(c)). One has to note that the preconditioning stage is controlled to ensure a quasi-static response of the system (the inertial number $I = \frac{\dot{\gamma} D_p}{P/\rho}$ is equal to 2.045×10^{-7} (MiDi, 2004)). The creep test being stress-controlled, the system response is directly related to the layer's dynamics (no numerical damping is used during this stage).

3 Macroscopic behaviors

The simulated emergent behavior show strong similarities with slip behaviors observed in laboratory (Scuderi et al., 2017; Scuderi & Collettini, 2018; Agliardi et al., 2020) and in situ (Guglielmi et al., 2015; Cappa et al., 2019) experiments under similar con-

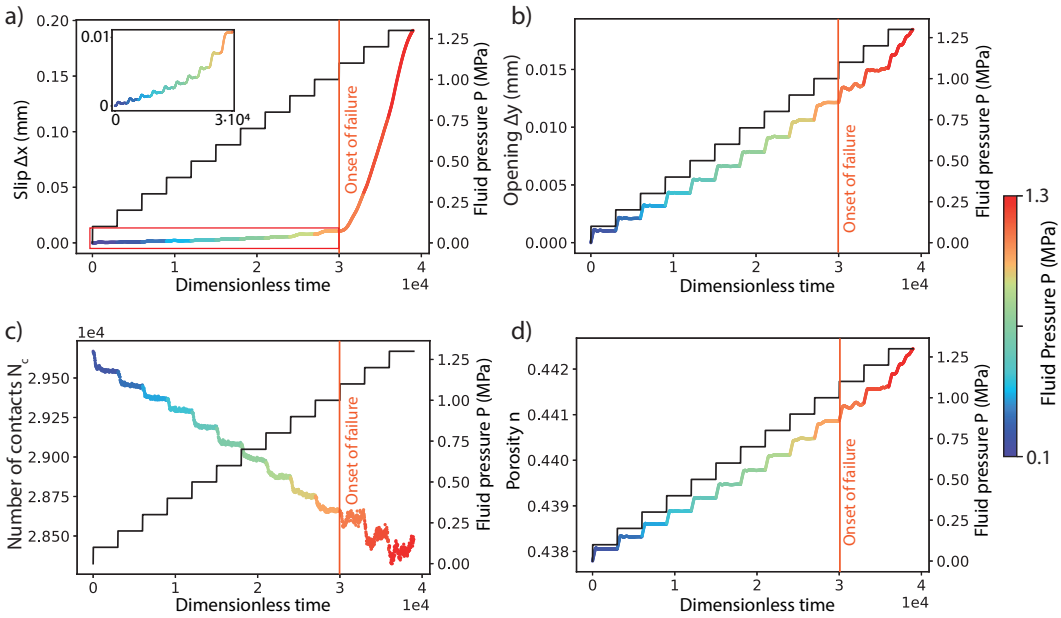

Figure 2. Response of the simulated shear zone during progressive fluid pressurization. (a) Shear displacement with a zoom up to the pre-failure state. (b) Normal displacement. (c) Total number of sphere-sphere contacts. (d) Evolution of the porosity. The curves are color-coded as functions of the fluid pressure P. Fluid pressure curves are plotted in black in each graph for reference.

ditions: slow steady slip is first observed up to the critical stress state ($\mu\sigma'_N \approx \tau_{ss}$) from which accelerated slip is then triggered. Those two stages have been assimilated by Scuderi et al. (Scuderi et al., 2017) respectively to the steady-state and unstable creep behaviors observed during secondary and tertiary creeps of intact rock (Brantut et al., 2013). Our simulation does not show any evidence of primary creep related compaction during the preconditioning stage of the loading as observed in (Scuderi et al., 2017). The compaction is most certainly related to time-dependent processes (*e.g.*, pressure solution) leading to grain to grain indentation that we did not take into account in our model formulation.

The first stage is characterized by a quasi-linear increase of both the shear and normal displacements as functions of the fluid pressure increase. Each pressure step produces an almost instantaneous acceleration of the system before it stabilizes to a new steady state (characterized by the successive plateaux on the curves). The amplitudes of the normal displacement steps remain proportional to the pressure increase over the entire stage (Figures 2(b)), while the amplitudes of the shear displacement steps tends to slightly increase as the system approaches the critical stress state (Figures 2(a)). Similarly to what was observed in the experiments of Scuderi et al. (Scuderi et al., 2017), the layer suffers a systematic overall dilation resulting from the fluid pressurization. The volumetric deformation of our numerical shear zone directly correlates to its opening and is proportional to the pressure increase (Figure 2(d)). This pressure induced dilation causes a progressive loss of interparticle contacts also proportional to the pressure increase, suggesting a redistribution of some interparticle forces into hydrostatic forces (Figure 2(c)).

The second stage is characterized by a rapid acceleration of slip that spontaneously evolves into dynamic failure as suggested by the slight decrease of shear stress described by the red portion of the curve in Figure 1(c). In agreement with the experiment done

by Scuderi et al. (Scuderi et al., 2017), the onset of failure corresponds almost exactly to the moment where the stress state approaches the critical stress state (the Mohr-Coulomb criterion). In contradiction to what was observed in the laboratory, the medium continuously dilates at a quasi-constant rate during this accelerated slip phase with, nonetheless, a slight acceleration after significant slip has developed (visible at the last pressure step, where P increases from 1.2 MPa to 1.3 MPa on Figure 2(b)). The lack of compaction during this accelerated slip stage is most certainly related to the fact that grain crushing is not possible in our numerical model while cataclasis and grain size reduction were systematically observed in the experiments. The oscillations in the evolution of both the opening and the number of contacts illustrate the dynamic and unstable nature of the response. The amplitudes of these oscillations are more pronounced than during the slow steady slip stage and suggest intense grains rearrangements within the medium.

We can summarize our results by saying that fluid pressurization induces slip well before reaching the critical steady-state strength. Slip remains slow and steady as long as this critical state is not reached. It accelerates to failure afterward, with some instabilities emerging from grain scale rearrangements. Dilation persists during the entire fluid pressurization and appears to develop at a quasi-constant rate, directly proportional to the pressure increase, whatever the emergent slip behavior.

The hydro-mechanical behaviors predicted by our numerical shear zone shows great similarities with behaviors observed both in laboratory and in situ on shear zones presenting different natures and subjected to different stress states (Guglielmi et al., 2015; Scuderi et al., 2017; Scuderi & Collettini, 2018; Cappa et al., 2019; Agliardi et al., 2020). Besides the relevance of the method itself and the confirmation that our DEM model constitutes a good analogue to study natural shear zones, our results confirm the consistency of shear zones' response to short term pore pressure variations despite the scale effect and the added complexity of natural environments.

4 Micromechanical processes

In order to get further insights into the mechanisms at work at the grain scale, we discretized the shear zone into 12 equal-sized sub-layers parallel to the shearing direction to estimate the vertical distributions of the quantities presented in Figure 2. Each layer is approximately 3 particles thick. The pressurization induced variations of slip, opening, number of contacts and porosity are presented in Figure 3 as vertical profiles corresponding respectively to 2 pre-failure states and 2 post-failure states (onset of failure occurs when the fluid pressure P increases from 1 MPa to 1.1 MPa).

In terms of displacements (Figures 3(a,b)), shear is preferentially localized within the shear band after failure. The profiles at sub-critical states (P=0.7 and 0.9 MPa) show slight but limited S-bend shapes compared to the post-failure states. The S-bend shape highlights the role of the shear band on the overall response and the relative passiveness of the surrounding bulk with regards to slip. A similar but less pronounced trend can be observed for the opening displacement profiles where inflexion points can be noticed at the shear band's boundaries. As observed macroscopically in Figures 2(a,b), the opening increments scale almost proportionally with the pore pressure increment at all stages, in contrast with the exponential increase of the post-failure slip increments.

The variations of the number of contacts and porosity (Figures 3(cd)) clearly point out to 2 different mechanisms representative respectively of (i) the slow and steady pre-failure creep, and (ii) the accelerated and dynamic post-failure slip. Both quantities evolve quasi-monotonically before failure across the entire layer, indicating an homogeneous response of the bulk to the pressurization: every increment of pore pressure leads to a loss of contacts as well as to a porosity increase which, as suggested by the macroscopic responses (Figures 2(cd)), are almost proportional to the pressure increase. After failure

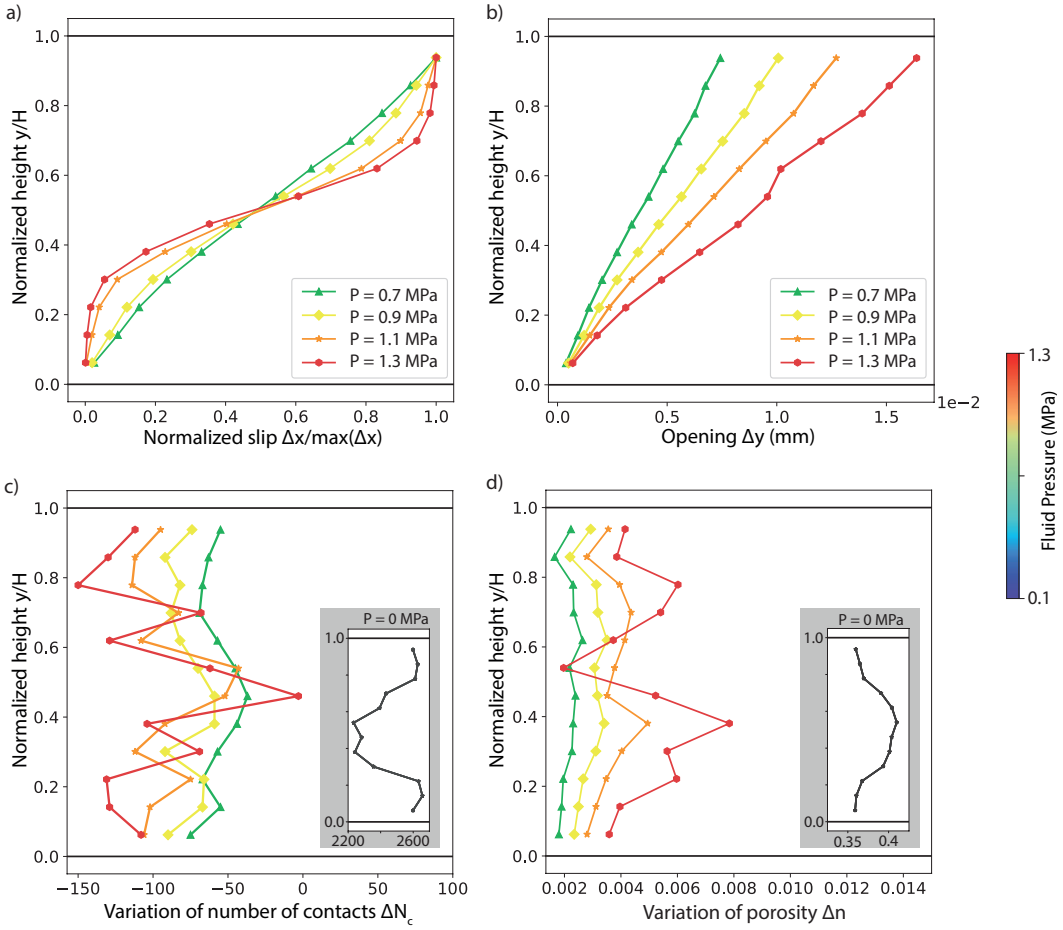

Figure 3. Profiles showing the vertical variation distributions of: (a) normalized slip, (b) opening, (c) number of contacts and (d) porosity within the shear zone at different stages of the fluid pressurization. The curves are color-coded as functions of the fluid pressure. Onset of failure occurs when the fluid pressure P increases from 1 MPa to 1.1 MPa. Inset figures in c) and d) show the vertical distributions of both the number of contacts and the porosity at the initial state, before fluid pressurization (P=0).

(P>1.1 MPa), both quantities highlight a localization of the deformation inside the shear band where contacts are gained and porosity decreases as described by the clear mid-height spike observed at P=1.3 MPa in both profiles. This indicates shear induced compaction within the shear band. Interestingly, the evolutions of both quantities outside the shear band follow the trends observed prior to failure, namely, loss of contacts and porosity increase. The coexistence of these somewhat opposite volumetric trends in and out of the shear band suggests deformation mechanisms taking place at the interfaces between the bulk and the shear band where a large amount of the opening is accommodated as suggested by the 2 spikes in the porosity profile at P=1.3 MPa ($\frac{y}{H} \approx 0.4, 0.8$), in conjunction with a noticeable gain of contacts below these interfaces ($\frac{y}{H} \approx 0.3, 0.7$). These post-failure profiles suggest sharply defined sub-horizontal structures that could actually be assimilated to the so-called Y-shears commonly observed in sheared materials in natural context (Reinen, 2000) and in experiments, either in the laboratory (Scuderi & Collettini, 2018) or in numerical analogs (Morgan & Boettcher, 1999).

Our observations suggest a high degree of particle rearrangement once accelerated slip occurs, leading to the generation of a hyperactive layer (the shear band) effectively disconnected from the surrounding material by discrete structures. By tracking the rotation of particles during the reactivation process (Figure 4(a)), we confirm the micromechanisms at play: slow steady creep corresponds to bulk deformation due to interlocked particles, while accelerated dynamic slip is mainly accommodated by interparticle rolling concentrated within the shear band. As discussed by Morgan and Boettcher (Morgan & Boettcher, 1999), shear loads within granular materials are borne by chains of particles carrying high forces. These chains evolve during shear and eventually fail due to interparticle rolling. We posit that post-failure accelerated slip is triggered by the sudden collapse of these force chains (a mechanisms identified as force-chain buckling in the literature by, *e.g.*, (Tordesillas, 2007)) within the shear band. As shown in Figure 4(b), the interparticle contact forces align to the direction of the maximum principal stress for both pre-failure and post-failure states (inclined at approximately 45° to the loading direction). Strong force chains are predominantly located within the shear band before failure. The same strong force chains actually persist up to failure (Figure 4(b)) and disappear once failure occurs. Once particles start to roll, the entire shear band acts as a roller bearing which promotes slip of the surrounding bulk. One can note that the slip rate tends to stabilize once this roller bearing is activated. Strong interparticle forces still concentrate within the shear band as a result of its compaction, but in a more diffuse manner. Interestingly, the distribution of sliding contacts (Figure 4(c)) does not directly correlate with particle rotations, specially just before the onset of failure (P=1 MPa) where particles starts to slide intensively inside the shear band while interparticle slips were only scarcely distributed over the entire system at lower pore pressures (*e.g.*, P=0.7 MPa). These interparticle slips occurring inside the shear band just before the onset of failure are clear precursors of the force chain collapses that lead to particle rolling and overall failure. Post-failure, interparticle slips tend to occur mainly inside the shear band where most particle rearrangements are concentrated, but some particles also slip outside of the shear band.

To sum up, pre-failure slow steady creep is associated to diffuse bulk deformation while post-failure accelerated dynamic slip results from very localized deformation processes taking place within the shear band. Similarly to what was observed in laboratory experiments on a saturated granular till (Rathbun & Marone, 2010), the pressurization of the layer induces a progressive transition from distributed shear to localized deformation. Evidence of this bi-modal accomodation of slip has also been observed in dry serpentinite gouge by Reinen (Reinen, 2000) who concluded that the microstructures that form during shear may be used to identify the seismic behavior of natural fault zones. Our numerical results tend to confirm her conclusions stating that stable fault creep results from distributed deformation, while localized deformation favors unstable dynamic slip. Before failure, grain reorganizations are very limited and the overall response of the

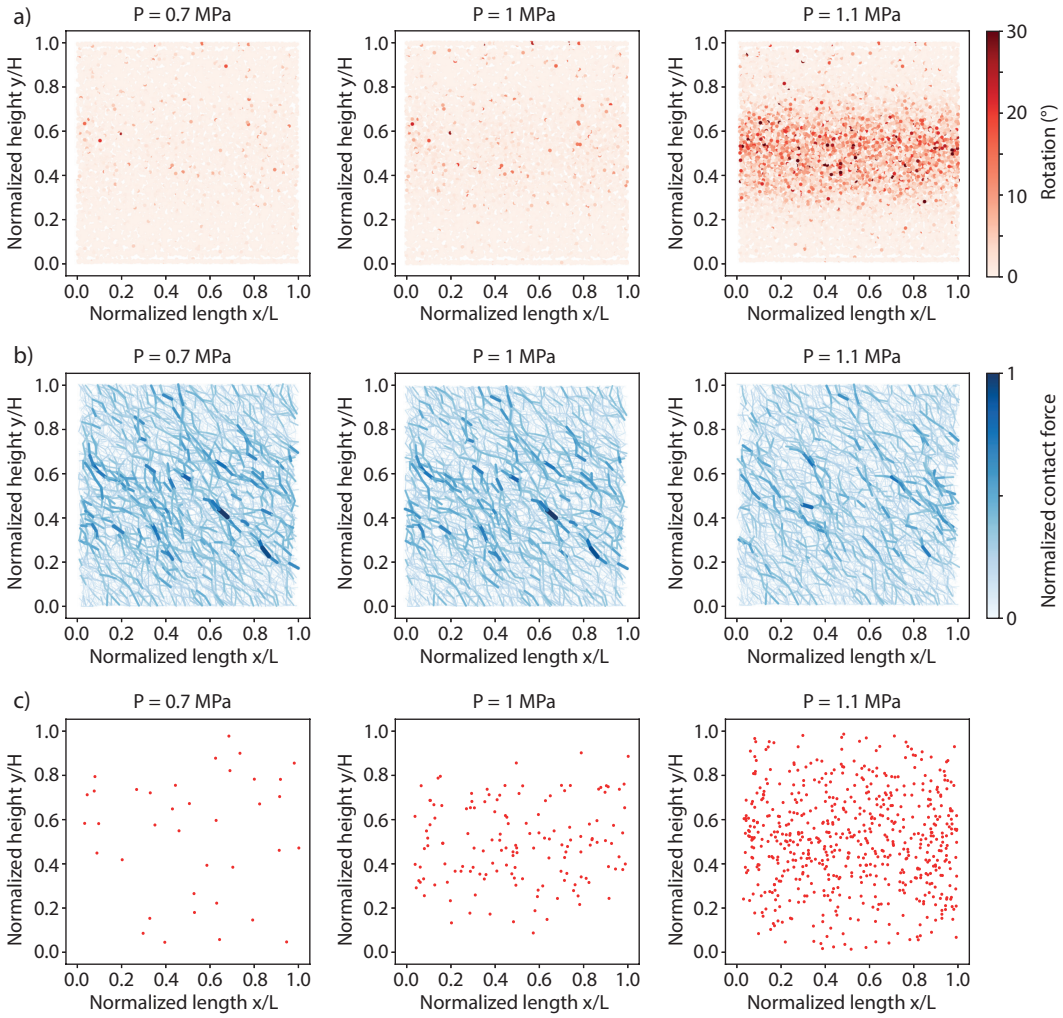

Figure 4. Microscale analyses on a vertical slice extracted from the sample at different stages of the reactivation: P = 0.7 MPa, P = 1 MPa, and P = 1.1 MPa. (a) Spatial distribution maps of accumulated particle rotations. (b) Interparticulate contact force network, color intensity and thicknesses of the line segments are proportional to the contact force magnitude. Normalized contact force is computed from all considered stages. (c) Spatial distribution of sliding contacts. Adjacent contacts with the two boundary walls are omitted to focus on what happens within the sample. Onset of failure occurs when the fluid pressure P was increased from 1 MPa to 1.1 MPa.

shear zone is driven by bulk deformation. Once failure occurs, the shear band concentrates all the grain rearrangements at the origin of the accelerated slip. As suggested by Morgan and Boettcher (Morgan & Boettcher, 1999), failure is directly correlated to grain rotations which promotes a dynamic response of the system.

5 Concluding remarks

We used a discrete element model to analyze the micromechanics of fluid induced reactivation of a granular shear zone under a sub-critical stress state. We were able to reproduce typical slip behaviors observed both in laboratory and in situ experiments: at constant shear stress, fluid pressurization reduces the normal stress and promotes slip through (i) slow steady slip before the critical state is reached, and (ii) accelerated dynamic slip afterward. Our micromechanical analysis show that these two slip behaviors are directly related to two distinct deformation modes: (i) a distributed mode where the entire layer deforms homogeneously in response to the pressure increase, and (ii) a localized mode where the shear band acts as a roller bearing for the surrounding bulk. The transition between these two deformation modes results from the rupture of interparticle force chains located within the shear band. By reducing the effective stress, fluid overpressurization promotes interparticle slips along these force chains which eventually lead to intense particle rearrangements once the critical stress state is reached. Pre-failure slip is mainly accomodated by dilation induced elastic shear distributed over the entire bulk, while post-failure slip is mainly accomodated through particle rolling located within the shear band. Our results suggest that grain rotations promote slip instabilities during fluid pressurization of granular shear zones.

Our numerical experiment constitutes a simplification of realistic configurations and it is evident that the simplicity of such an idealized system affect its mechanical behavior (*e.g.*, the sphericity of particles has a strong influence on the macroscopic volumetric deformations). Nonetheless, several studies have shown that discrete element models can be considered as a good first approximation to understand the complexity of the mechanisms that characterize shear zones during deformation (Morgan & Boettcher, 1999; Aharonov & Sparks, 2004; Mair & Hazzard, 2007; Rathbun et al., 2013). Even though the present study provides insight into the micromechanisms at work in pressurized granular shear zones, additional work is needed to fully characterize fluid induced slip behaviors in natural shear zones. For instance, beside the influence of key loading parameters such as the injection rate or the normal stress that needs to be investigated, the introduction of time-dependent physics in the model formulation as suggested for example by (Van Den Ende et al., 2018) would allow to discuss fluid induced slip behaviors in the context of the rate- and state- friction theory, while the consideration of crushable grains as proposed for example by (Abe & Mair, 2009) would give further insights into the deformation process since grain fracturing plays a key role in the evolution of gouge during shear.

Acknowledgments

This work was supported partly by the french PIA project “Lorraine Université d’Excellence”, reference ANR-15-IDEX-04-LUE. The source code of the YADE-DEM software used for the simulations in this study is available at https://yade-dem.org/doc/installation.html (Šmilauer et al., 2010).

References

Abe, S., & Mair, K. (2009). Effects of gouge fragment shape on fault friction: New 3d modelling results. *Geophysical Research Letters*, *36*(23). doi: 10.1029/2009GL040684

Agliardi, F., Scuderi, M. M., Fusi, N., & Collettini, C. (2020). Slow-to-fast transition of giant creeping rockslides modulated by undrained loading in basal shear zones. *Nature Communications*, *11*(1), 1352. doi: 10.1038/s41467-020-15093-3

Aharonov, E., & Scholz, C. H. (2018). A physics-based rock friction constitutive law: Steady state friction. *Journal of Geophysical Research: Solid Earth*, *123*(2), 1591-1614. doi: 10.1002/2016JB013829

Aharonov, E., & Sparks, D. (2004). Stick-slip motion in simulated granular layers. *Journal of Geophysical Research: Solid Earth*, *109*(B9). doi: 10.1029/2003JB002597

Boulton, G. S., & Hindmarsh, R. C. A. (1987). Sediment deformation beneath glaciers: Rheology and geological consequences. *Journal of Geophysical Research: Solid Earth*, *92*(B9), 9059-9082. doi: 10.1029/JB092iB09p09059

Brantut, N., Heap, M. J., Meredith, P. G., & Baud, P. (2013). Time-dependent cracking and brittle creep in crustal rocks: A review. *Journal of Structural Geology*, *52*, 17-43. doi: 10.1016/j.jsg.2013.03.007

Cappa, F., Guglielmi, Y., Viseur, S., & Garambois, S. (2014). Deep fluids can facilitate rupture of slow-moving giant landslides as a result of stress transfer and frictional weakening. *Geophysical Research Letters*, *41*(1), 61-66. doi: 10.1002/2013GL058566

Cappa, F., Scuderi, M. M., Collettini, C., Guglielmi, Y., & Avouac, J.-P. (2019). Stabilization of fault slip by fluid injection in the laboratory and in situ. *Science Advances*, *5*(3), eaau4065.

Catalano, E., Chareyre, B., & Barthélémy, E. (2014). Pore-scale modeling of fluid-particles interaction and emerging poromechanical effects. *International Journal for Numerical and Analytical Methods in Geomechanics*, *38*(1), 51-71. doi: 10.1002/nag.2198

Chareyre, B., Cortis, A., Catalano, E., & Barthélemy, E. (2012). Pore-Scale Modeling of Viscous Flow and Induced Forces in Dense Sphere Packings. *Transport in Porous Media*, *92*(2), 473-493. doi: 10.1007/s11242-011-9915-6

Cornet, F. H., Helm, J., Poitrenaud, H., & Etchecopar, A. (1998). Seismic and aseismic slips induced by large-scale fluid injections. In S. Talebi (Ed.), *Seismicity associated with mines, reservoirs and fluid injections* (p. 563-583). Basel: Birkhäuser Basel.

Cundall, P. A., & Strack, O. D. L. (1979). A discrete numerical model for granular assemblies. *Géotechnique*, *29*(1), 47-65. doi: 10.1680/geot.1979.29.1.47

Dieterich, J. H. (1979). Modeling of rock friction: 1. experimental results and constitutive equations. *Journal of Geophysical Research: Solid Earth*, *84*(B5), 2161-2168. doi: 10.1029/JB084iB05p02161

Dorostkar, O., Guyer, R. A., Johnson, P. A., Marone, C., & Carmeliet, J. (2017). On the micromechanics of slip events in sheared, fluid-saturated fault gouge. *Geophysical Research Letters*, *44*(12), 6101-6108. doi: 10.1002/2017GL073768

Ferdowsi, B., Griffa, M., Guyer, R. A., Johnson, P. A., Marone, C., & Carmeliet, J. (2013). Microslips as precursors of large slip events in the stick-slip dynamics of sheared granular layers: A discrete element model analysis. *Geophysical Research Letters*, *40*(16), 4194-4198. doi: 10.1002/grl.50813

Ferdowsi, B., & Rubin, A. M. (2020). A granular physics-based view of fault friction experiments. *Journal of Geophysical Research: Solid Earth*, *125*(6), e2019JB019016. doi: 10.1029/2019JB019016

Guglielmi, Y., Cappa, F., Avouac, J.-P., Henry, P., & Elsworth, D. (2015). Seismicity triggered by fluid injection–induced aseismic slip. *Science*, *348*(6240), 1224-1226. doi: 10.1126/science.aab0476

Hazzard, J. F., & Mair, K. (2003). The importance of the third dimension in granular shear. *Geophysical Research Letters*, *30*(13). doi: 10.1029/2003GL017534

King Hubbert, M., & Rubey, W. W. (1959). Role of fluid pressure in mechanics of

overthrust faulting: I. mechanics of fluid-filled porous solids and its application to overthrust faulting. *Geological Society of America Bulletin*, *70*(2), 115-166.

Linker, M. F., & Dieterich, J. H. (1992). Effects of variable normal stress on rock friction: Observations and constitutive equations. *Journal of Geophysical Research: Solid Earth*, *97*(B4), 4923-4940. doi: 10.1029/92JB00017

Mair, K., & Hazzard, J. F. (2007). Nature of stress accommodation in sheared granular material: Insights from 3d numerical modeling. *Earth and Planetary Science Letters*, *259*(3), 469-485. doi: 10.1016/j.epsl.2007.05.006

Mathews, W. H. (1964). Water pressure under a glacier. *Journal of Glaciology*, *5*(38), 235-240. doi: 10.3189/S0022143000028811

MiDi, G. (2004). On dense granular flows. *The European Physical Journal E*, *14*, 341-365. doi: 10.1140/epje/i2003-10153-0

Šmilauer, V., Catalano, E., Chareyre, B., Dorofeenko, S., Duriez, J., Gladky, A., ... others (2010). Yade reference documentation. *Yade Documentation*, *474*(1).

Morgan, J. K., & Boettcher, M. S. (1999). Numerical simulations of granular shear zones using the distinct element method: 1. shear zone kinematics and the micromechanics of localization. *Journal of Geophysical Research: Solid Earth*, *104*(B2), 2703-2719. doi: 10.1029/1998JB900056

Rathbun, A. P., & Marone, C. (2010). Effect of strain localization on frictional behavior of sheared granular materials. *Journal of Geophysical Research: Solid Earth*, *115*(B1). doi: 10.1029/2009JB006466

Rathbun, A. P., Renard, F., & Abe, S. (2013). Numerical investigation of the interplay between wall geometry and friction in granular fault gouge. *Journal of Geophysical Research: Solid Earth*, *118*(3), 878-896. doi: 10.1002/jgrb.50106

Rattez, H., Shi, Y., Sac-Morane, A., Klaeyle, T., Mielniczuk, B., & Veveakis, M. (2020). Effect of grain size distribution on the shear band thickness evolution in sand. *Géotechnique*, *0*(0), 1-39. doi: 10.1680/jgeot.20.P.120

Reinen, L. A. (2000). Seismic and aseismic slip indicators in serpentinite gouge. *Geology*, *28*(2), 135-138. doi: 10.1130/0091-7613(2000)28<135:SAASII>2.0.CO;2

Ruina, A. (1983). Slip instability and state variable friction laws. *Journal of Geophysical Research: Solid Earth*, *88*(B12), 10359-10370. doi: 10.1029/JB088iB12p10359

Scholtès, L., Chareyre, B., Michallet, H., Catalano, E., & Marzougui, D. (2015). Modeling wave-induced pore pressure and effective stress in a granular seabed. *Continuum Mechanics and Thermodynamics*, *27*(1), 305-323. doi: 10.1007/s00161-014-0377-2

Scholz, C. (1998). Earthquakes and friction laws. *Nature*, *391*, 37-42. doi: 10.1038/34097

Scuderi, M., & Collettini, C. (2016). The role of fluid pressure in induced vs. triggered seismicity: insights from rock deformation experiments on carbonates. *Scientific Reports*, *6*(24852). doi: 10.1038/srep24852

Scuderi, M., & Collettini, C. (2018). Fluid Injection and the Mechanics of Frictional Stability of Shale-Bearing Faults. *Journal of Geophysical Research: Solid Earth*, *123*(10), 8364-8384. doi: 10.1029/2018JB016084

Scuderi, M., Collettini, C., & Marone, C. (2017, November). Frictional stability and earthquake triggering during fluid pressure stimulation of an experimental fault. *Earth and Planetary Science Letters*, *477*, 84-96. doi: 10.1016/j.epsl.2017.08.009

Segall, P., & Rice, J. R. (1995). Dilatancy, compaction, and slip instability of a fluid-infiltrated fault. *Journal of Geophysical Research: Solid Earth*, *100*(B11), 22155-22171. doi: 10.1029/95JB02403

Tordesillas, A. (2007). Force chain buckling, unjamming transitions and shear banding in dense granular assemblies. *Philosophical Magazine*, *87*(32), 4987-5016. doi: 10.1080/14786430701594848

Van Den Ende, M. A., Marketos, G., Niemeijer, A., & Spiers, C. (2018). Investigating compaction by intergranular pressure solution using the discrete element method. *Journal of Geophysical Research: Solid Earth*, *123*(1), 107-124. doi: 10.1002/2017JB014440

Yang, Z., & Juanes, R. (2018, Feb). Two sides of a fault: Grain-scale analysis of pore pressure control on fault slip. *Physical Review E*, *97*, 022906. doi: 10.1103/PhysRevE.97.022906

Supporting Information for "Micromechanics of sheared granular layers activated by fluid pressurization"

Hien Nho Gia Nguyen[1], Luc Scholtès[1,2], Yves Guglielmi[3], Frédéric Victor Donzé[4], Zady Ouraga[5], Mountaka Souley[5]

[1]Université de Lorraine, CNRS, GeoRessources, Nancy, France

[2]Université Clermont Auvergne, CNRS, IRD, OPGC, Laboratoire Magmas et Volcans, Clermont-Ferrand, France

[3]Lawrence Berkeley National Laboratory, Energy Geosciences Division, Berkeley, CA, USA

[4]Université Grenoble-Alpes, CNRS, ISTerre, Grenoble, France

[5]Ineris, Verneuil-en-Halatte, France

Contents of this file

1. DEM-PFV formulations

The numerical sample consists of smooth spherical particles. The DEM module handles the solid phase while the PFV module handles the fluid phase.[1] The DEM is based on a Lagrangian approach where each particle is identified by its own mass, size and moment of inertia. The computation scheme consists in integrating Newton's second law so as to determine particles motion and interactions one with another. The DEM model is a 3D implementation in the open source code YADE-DEM where interparticle contacts are modeled by linear elastic relationships between forces and interparticle displacements, associated with a slip Coulomb model. The contact laws governing the interactions are defined from 3 parameters including the normal stiffness coefficient k_n, the tangent stiffness coefficient k_t and the microscopic friction coefficient μ_p (Cundall & Strack, 1979). The inter-particle contact behavior have two components: (1) the normal contact is governed by an elastic force-displacement relation $\Delta F_n = k_n \Delta \delta_c \geq 0$ where δ_c is the overlapping between two particles in contact; (2) the tangent force is incrementally computed at each numerical time step as $\Delta F_t = k_t \Delta u_t$ and $|F_t| \leq F_n \tan \mu_p$. The parameters for the contact laws are given in Table S1. The numerical sample consists of 12,000 spherical particles with a uniform size distribution whose diameters vary between 0.066 mm and 0.133 mm with the density of 2600 kg/m^3. The microscopic friction coefficient μ_p is 0.52.

For the fluid coupling, the PFV module is able to describe the compressible flow at the particle scale in the viscous regime. A partition of the pore space is obtained by constructing the regular triangulation of the packing. The elementary objects emerging from this procedure are tetrahedrons whose vertices are defined by the centers of gravity

of the particles. The space limited by this structure is known as the pore space. For the sake of simplicity, the information in this document is a summary extracted from (Scholtès et al., 2015). More details of the PFV formulation can be found in (Chareyre et al., 2012).

Let us define Ω_i the portion of the pore i occupied by the fluid (Figure S1). Integrating the continuity equation in Ω_i gives:

$$\int_{\Omega_i} \frac{\partial \rho_\mathrm{f}}{\partial t} \mathrm{d}V = -\int_{\Omega_i} \nabla \cdot (\rho_\mathrm{f} \mathbf{v})\, \mathrm{d}V \tag{1}$$

where ρ_f is the fluid density and $\mathbf{v}$ is the fluid velocity. Applying the divergence theorem leads Eq. (1) to

$$\int_{\Omega_i} \frac{\partial \rho_\mathrm{f}}{\partial t} \mathrm{d}V = -\int_{\partial\Omega_i} \rho_\mathrm{f} \mathbf{v} \cdot \mathbf{n} \mathrm{d}S \tag{2}$$

with $\mathbf{n}$ the outward pointing unit vector normal to $\partial\Omega_i$. As the vertices of the elements follow the motion of the particles, the element is deforming at a certain rate. Introducing $\mathbf{u}$ as the velocity of the contour $\partial\Omega_i$, Eq. (2) can be written as:

$$\int_{\Omega_i} \frac{\partial \rho_\mathrm{f}}{\partial t} \mathrm{d}V = -\int_{\partial\Omega_i} \rho_\mathrm{f} (\mathbf{v} - \mathbf{u}) \cdot \mathbf{n} \mathrm{d}S - \int_{\partial\Omega_i} \rho_\mathrm{f} \mathbf{u} \cdot \mathbf{n} \mathrm{d}S \tag{3}$$

The bulk modulus K_f relates the time derivatives of ρ_f and P_i as

$$K_\mathrm{f} = \rho_\mathrm{f} \frac{\partial P_i}{\partial \rho_\mathrm{f}}, \tag{4}$$

for a compressible fluid.

For saturated media (degree of saturation $S_r = 1$), K_f is equal to the fluid bulk modulus (e.g. water $K_w = 2.2 \times 10^9$ Pa). If air phase is available in the fluid ($0.9 < S_r < 1$), K_f depends on the gaz content in the fluid mixture:

$$K_\mathrm{f} = \frac{1}{\dfrac{S_r}{K_\mathrm{w}} + \dfrac{1 - S_r}{K_\mathrm{a}}} \tag{5}$$

assuming the air distribution within fluid is uniform in all pores, with K_a the bulk modulus of air.

Considering Eq. (4) and neglecting the spatial fluctuation of ρ_f in the vicinity of the domain (small Mach number), Eq. (3) thus becomes

$$\int_{\Omega_i} \frac{1}{K_\mathrm{f}} \frac{\partial P_i}{\partial t} \mathrm{d}V = -\sum_{j=1}^{4} \int_{S_{ij}^f} (\mathbf{v} - \mathbf{u}) \cdot \mathbf{n} \mathrm{d}S - \dot{V}_{p,i} \tag{6}$$

where $\dot{V}_{p,i}$ is the time derivative of the pore volume and S_{ij}^f is the intersection of the triangular surface with the fluid domain along each side of the tetrahedron.

The fluxes integrals appearing on the right-hand side of Eq(6) can be linked to the pressure jump between two pores i and j so that the equation becomes

$$\dot{P}_i = -\frac{K_\mathrm{f}}{V_{f,i}} \left[\dot{V}_{p,i} + \sum_{j=1}^{4} k_{ij} \left(P_i - P_j \right) \right] \tag{7}$$

with k_{ij} the conductivity of the thoat between i and j, k_{ij} being computed as a function of the thoat geometry through a generalized Poiseuille's law.

A finite difference discretization of Eq. (7) using a backward Euler scheme for the evaluation of $\dot{P}_i$ gives

$$\sum_{j=1}^{4} k_{ij} P_j^t - \left(\zeta_i + \sum_{j=1}^{4} k_{ij} \right) P_i^t = \dot{V}_{p,i}^{t-1/2} - \zeta_i P_i^{t-1}, \quad \text{with} \quad \zeta_i = \frac{V_{f,i}}{K_\mathrm{f} \Delta t} \tag{8}$$

where the time-centered evaluation of $\dot{V}_{p,i}^{t-1/2}$ is obtained from mid-step velocities of the particles. An implicit scheme is obtained by considering Eq. (8) for all pores at a given time. The associated linear system has to be solved as each time-step of the simulation, linking the pressure field P^t to the deformation rate of the pore space.

In turn, the force exerted by the fluid on each particle p can be deduced using the same expressions as for an incompressible fluid. It is the sum of three terms which are contour integrals of the hydrostatic pressure $\rho_\mathrm{f} g z$ (buoyancy), of the piezometric pressure P and the viscous shear stress $\boldsymbol{\tau}$, respectively:

$$\mathbf{F}^p = \int_{\Gamma_p} \rho_\mathrm{f} g z \mathbf{n} \mathrm{d}S + \int_{\Gamma_p} P \mathbf{n} \mathrm{d}S + \int_{\Gamma_p} \tau \mathbf{n} \mathrm{d}S = \mathbf{F}^{B,p} + \mathbf{F}^{P,p} + \mathbf{F}^{V,p}, \tag{9}$$

Γ_p is the solid surface of the particle p. These forces are determined for time t and integrated into the conventional explicit time-stepping algorithm of the DEM by summing them together with the contact forces. This sequence of equations (8) and (9) defines a semi-implicit integration scheme.

2. Analysis methods

2.1. Extracting sub-sample

While the numerical sample is three dimensional and it has periodic boundaries on the horizontal directions, a vertical slide with thickness of about 15 particles is sufficient for the analysis. This sub-sampling method allows the efficiency of the analysis while maintain the clearance of data visualization by projecting 3D data point on a 2D diagram.

2.2. Particle rotation calculation

The accumulated rotation of the particle is calculated from the snapshots of the sample between two stages: the current selected stage versus the initial stage where the fluid injection starts (P = 0 MPa).

2.3. Contact force network

The contact force network is a set of particle-particle interactions visualized based on the position of the grains in contact and the intensity of their local contact force. At a selected stage, normal contact forces of all interaction can be computed as mentioned in Section 1. The line segments represent the vector branch connecting two particles in contact. For the normalization, the max and min of normal contact forces from all three stages are taken into account. Then, the normalization is based on these max and min values, enabling a consistent comparison method.

2.4. Sliding contact detection

For a particle-particle interaction, when the computed tangent force F_t exceeds the threshold $F_n \tan \mu_p$, the contact is defined as a 'sliding contact'. The position of a sliding contact is the midpoint of two involved particles. It worths noting that it is expected to have high amount of sliding contacts at the boundaries (top and bottom plates) because of the shear control is governed by the plate movement. Hence, in order to focus better on what happens within the sample, especially around the shear band, the sliding contacts near the boundaries are not displayed.

References

Chareyre, B., Cortis, A., Catalano, E., & Barthélemy, E. (2012). Pore-Scale Modeling of Viscous Flow and Induced Forces in Dense Sphere Packings. *Transport in Porous Media*, *92*(2), 473-493. doi: 10.1007/s11242-011-9915-6

Cundall, P. A., & Strack, O. D. L. (1979). A discrete numerical model for granular assemblies. *Géotechnique*, *29*(1), 47-65. doi: 10.1680/geot.1979.29.1.47

Scholtès, L., Chareyre, B., Michallet, H., Catalano, E., & Marzougui, D. (2015). Modeling wave-induced pore pressure and effective stress in a granular seabed. *Continuum Mechanics and Thermodynamics*, *27*(1), 305-323. doi: 10.1007/s00161-014-0377-2

Notes

1. DEM: discrete elements method, PFV: pore-scale finite volume

Table S1. Model properties

Particles and contacts	**value**	**Bulk (steady-state)**	**value**
Particle diameter D_p	$0.1 \pm 0.033\,\mathrm{mm}$	Porosity n	0.438
Particle density ρ_p	$2{,}600\,\mathrm{kg/m^3}$	Permeability $k_x = k_z = 2k_y$	$2.4 \cdot 10^{-11}\,\mathrm{m^2}$
Normal stiffness $\frac{k_n}{D_p}$	$1\,\mathrm{GPa}$	Normal stiffness K_n	$20.9\,\mathrm{MPa{\cdot}m}$
Shear stiffness $\frac{k_s}{D_p}$	$0.25\,\mathrm{GPa}$	Shear stiffness K_s	$5\,\mathrm{MPa{\cdot}m}$
Friction coefficient μ_p	0.52	Friction coefficient μ	0.38 ± 0.01

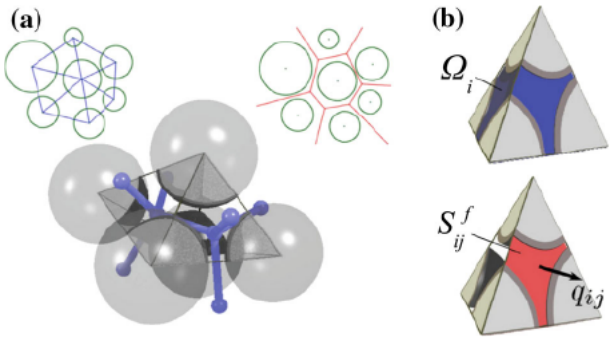

Figure S1. (a) Regular triangulation and its dual Voronoi's graph in two dimensional and in three dimensional. (b) Elementary fluid domain (tetrahedron) in triangulated sphere assembly.